

Imaging Organophosphate and Pyrophosphate Sequestration on Brucite by in Situ Atomic Force Microscopy

Lijun Wang,^{*,†,‡} Christine V. Putnis,^{*,‡,§} Helen E. King,^{||} Jörn Hövelmann,^{⊥,¶} Encarnación Ruiz-Agudo,[#] and Andrew Putnis^{‡,▽}

[†]College of Resources and Environment, Huazhong Agricultural University, Wuhan 430070, China

[‡]Institut für Mineralogie, University of Münster, 48149 Münster, Germany

[§]Department of Chemistry, Curtin University, Perth, Western Australia 6845, Australia

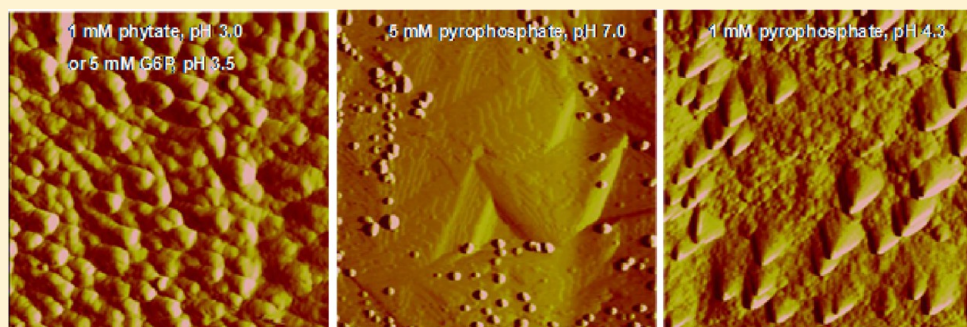
^{||}Department of Earth Sciences, Utrecht University, 3584 CD Utrecht, The Netherlands

[⊥]Interface-Geochemistry, Geoforschungszentrum Potsdam, Telegrafenberg, 14473 Potsdam, Germany

[#]Department of Mineralogy and Petrology, University of Granada, Fuentenueva s/n, Granada 18071, Spain

[▽]The Institute for Geoscience Research (TIGeR), Curtin University, Perth, Western Australia 6102, Australia

S Supporting Information



ABSTRACT: In order to evaluate the organic phosphorus (OP) and pyrophosphate (PyroP) cycle and their fate in the environment, it is critical to understand the effects of mineral interfaces on the reactivity of adsorption and precipitation of OP and PyroP. Here, in situ atomic force microscopy (AFM) is used to directly observe the kinetics of coupled dissolution–precipitation on cleaved (001) surfaces of brucite [Mg(OH)₂] in the presence of phytate, glucose-6-phosphate (G6P) and pyrophosphate, respectively. AFM results show that the relative order of contribution to mineral surface adsorption and precipitation is phytate > pyrophosphate > G6P under the same solution conditions and can be quantified by the induction time of OP/PyroP–Mg nucleation in a boundary layer at the brucite–water interface. Calculations of solution speciation during brucite dissolution in the presence of phytate or pyrophosphate at acidic pH conditions show that the solutions may reach supersaturation with respect to Mg₅H₂Phytate·6H₂O as a Mg-phytate phase or Mg₂P₂O₇ as a Mg-pyrophosphate phase that becomes thermodynamically stable before equilibrium with brucite is reached. This is consistent with AFM dynamic observations for the new phase formations on brucite. Direct nanoscale observations of the transformation of adsorption/complexation–surface precipitation, combined with spectroscopic characterizations and species simulations may improve the mechanistic understanding of organophosphate and pyrophosphate sequestration by mineral replacement reactions through a mechanism of coupled dissolution–precipitation occurring at mineral–solution interfaces in the environment.

INTRODUCTION

Phosphorus (P) is a major growth limiting nutrient of plants and other organisms, and elevated P inputs into soil solutions and aquatic environments leads to eutrophication, therefore increasing the risk of environmental pollution.¹ In waters and sediments, dissolved or particulate organic phosphorus (OP) is found in similar amounts to inorganic P.² Moreover, OP was recently proposed as a potential pool for bioavailable P, promoting much research regarding OP decomposition,³ fractionation,^{4,5} and characterization.⁶

OP forms include phosphonates, myo-inositol hexakisphosphate, and orthophosphate mono(di)esters.⁷ Phosphomonoesters in supra-/macro-molecular structures were found to account for the majority of soil OP across diverse soils.⁸ A considerable proportion of OP in soils or wetlands occurs as stereoisomers of inositol hexakisphosphate (IP6).⁹ The most

Received: October 27, 2016

Revised: December 7, 2016

Accepted: December 8, 2016

Published: December 8, 2016

abundant *myo*-IP6 occurs as a phosphorus storage compound in seeds.^{10,11} When IP6 chelates metals such as Ca, Mg, or Fe it forms an insoluble phytate, for example the common cereal component phytin (Ca–Mg–K phytate).^{12,13} Phytate has also been detected in plant root exudates.^{14,15} Glucose-6-phosphate (G6P), a representative sugar monoester, has also been detected in soils.¹⁶

In addition to OPs, increased amounts of pyrophosphate form after pyrolysis of raw sewage sludge,¹⁷ and pyrophosphate is present in aquatic ecosystems including marine particulates¹⁸ and estuary sediments,¹⁹ and also is common in soil samples.²⁰ The function of pyrophosphate in terrestrial and aquatic P cycles is unclear, though it has been shown to be bioavailable even in the presence of high ambient soluble reactive P.¹⁹

Most inorganic phosphorus (IP) and OP in soils, eutrophic water bodies or sewage sludges are present as surface adsorbed species on minerals.^{21,22} The concentrations of both dissolved (DP) and particulate phosphorus (PP) are correlated with the organic component concentration²³ in sediment containing different mineral components.²⁴ Various OP and IP compounds including PyroP in these natural environments exhibit significant differences in their chemical behavior with mineral surfaces, reactivity and bioavailability.²⁵

OP and PyroP constitute a major component of soil phosphorus and play a key role in the P cycle.²⁶ Therefore, the dynamics of OP and PyroP in the environment,²⁷ particularly the kinetics associated with OP/PyroP-mineral surface reactions, including adsorption, complexation and precipitation, will play a significant role in the biogeochemistry of these molecules and their fate in different ecosystems.²⁷ Although the roles of different mineral surfaces in OP and PyroP adsorption and immobilization have been widely studied, little is known regarding the kinetics of dissolution and precipitation at the brucite mineral-solution interface. As a model mineral, brucite was chosen because (1) it exhibits a simple composition and structure and could be an analogue for brucite-like minerals such as hydrotalcite-like layered double hydroxides (LDHs that include clay minerals) with a high chemical affinity for both OP and PyroP; (2) dissolution and precipitation reactions at the brucite-solution interface occur easily within the AFM experimental time frame. Therefore, the objective of this study was to observe the kinetic processes of brucite dissolution in the presence of phytate, G6P, and pyrophosphate and coupled precipitation. In addition, we aimed to determine how the number of phosphate groups in molecules regulates complexation of OP/PyroP-Mg and subsequent precipitation, providing insights into the fundamental mineral interfacial phenomenon in controlling OP and PyroP sequestration in the environment.

■ EXPERIMENTAL SECTION

Brucite Dissolution. In situ dissolution experiments were performed using a Digital Instruments (Bruker) Nanoscope IIIa AFM (Multimode) operating in contact mode. A natural optically clear brucite crystal (Norberg, Sweden) was cleaved in order to expose a fresh cleavage (001) surface. The brucite was characterized as single phase by X-ray diffraction. The solutions of phytate, G6P, and pyrophosphate (0.01 to 5.0 mM) at different pH values (2.7–9.6), adjusted by the addition of 0.01 M NaOH or HCl, were passed over the cleaved brucite crystals in the AFM fluid cell. NaCl (1.0–100.0 mM at pH 7.0) was added to the phytate or pyrophosphate solutions (1.0 mM) to observe the effects of ionic strength on brucite dissolution. In

situ experiments were conducted at a constant flow rate of 1 mL/min to ensure surface-controlled reaction rather than diffusion (transport) control. Different locations of three different crystals per solution condition were imaged to ensure reproducibility of the results. In the present study, the formation of precipitates followed brucite dissolution; thus we used the time before the first particles (about 2.0–6.0 nm in height) were observed on the brucite surface to characterize the kinetics of nucleation.

Ex situ dissolution experiments (0.1–1.0 mM phytate at pH 2.7–3.7, 1.0 mM pyrophosphate at pH 4.3, and 5.0 mM G6P at pH 3.5) were performed following in situ AFM experiments. The reacted brucite samples were removed from the AFM fluid cell and placed in a beaker filled with about 10 mL of the different solutions at room temperature for 16–24 h in order to observe further precipitation reactions. After 16 or 24 h, the samples were removed from the solution and quickly dried using absorbent paper and then immediately imaged in the AFM.

Raman Spectroscopy. Raman spectra were collected using a WITec Alpha 300R confocal Raman spectrometer operating with the 785 nm line of a diode laser. A 50x long working distance lens (NA 0.5) was used to obtain spatially constrained information from surface precipitates produced during the AFM and batch experiments. As the precipitates were sensitive to the laser beam, the laser intensity was lowered until no change was observed optically or in the spectrum. Depth scans of the surfaces were taken using with an integration time of 3 s. The brucite spectrum was generated from an average of four spectra taken from 5 μm below the surface. After positions were identified with additional peaks not related to brucite at the surface, longer collection times were used to help identify the precipitates. Single spectra were taken for 3 s and integrated 30 times to obtain the best signal-to-noise ratio. All spectra were obtained using a grating of 300 grooves/mm and a pinhole of 20 μm . Spectral background removal and peak fitting was conducted using the WITec Project Plus software (version 4.0).

Scanning Electron Microscopy (SEM). Imaging of the phases precipitated at the brucite surfaces was conducted using a FEI Helios Nanolab G3 SEM. Images of the surface precipitates were taken at 10 kV acceleration voltage and 0.8 nA probe current.

PHREEQC Simulations. The PHREEQC program²⁸ was used to simulate the reactions between brucite and OP/PyroP solutions using the database wateq.dat. First, we calculated the solution speciation using thermodynamic constants (Supporting Information (SI) Table S1–S7) during brucite dissolution in the presence of 1.0 mM phytate at pH 2.5 and 7.0 by PHREEQC. This provided simulations of brucite dissolving until equilibrium with the solution was reached. For the pyrophosphate system (1.0 mM) at more acidic pH (4.3) conditions the solution reaches saturation with respect to $\text{Mg}_2\text{P}_2\text{O}_7$ as a Mg-pyrophosphate phase. Moreover, we made further simulations for the same solutions of 1.0 mM phytate and pyrophosphate at a fixed pH of 4.3 or 7.0, while allowing the pH to vary as brucite dissolved.

■ RESULTS AND DISCUSSION

Coupled Dissolution–Precipitation at the Brucite–Solution Interface in the Presence of Phytate. Following 329 s of injection of 1 mM phytate (pH 9.0), slow dissolution occurred on the exposed (001) surfaces with the formation of shallow, equilateral triangular etch pits with a depth of 0.5–1.0

nm (Figure 1A, B). Pit depth increased to about 1.5 nm and 2.5–3.0 nm after 7 and 43 min, respectively (Figure 1C, D).

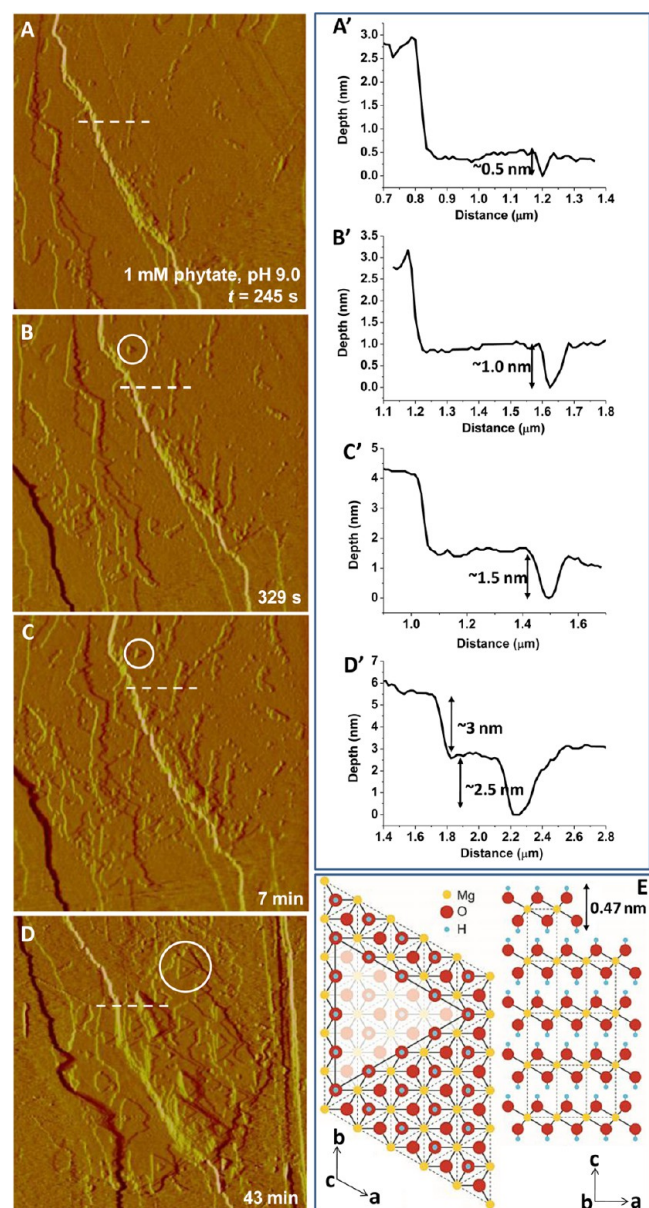


Figure 1. Time sequence AFM (deflection mode) images of natural brucite dissolution. (A–D) Time-lapse images show equilateral triangular etch pit formation and evolution on the (001) cleavage plane (the white circles in B–D) after injection of 1 mM phytate (pH 9.0) into a flow-through cell. Images A–C, $3 \times 3 \mu\text{m}$; D, $5 \times 5 \mu\text{m}$. (A'–D') Depth profile of the etch pit at $t = 245$ s, 329 s, 7 min, or 43 min, respectively, measured along the white dashed lines in (A–D). (E) The brucite atomic structure projected along the b -axis (in right panel of E; 0.47 nm of the thickness of one $\text{Mg}(\text{OH})_2$ layer), and the c -axis (in left panel of E; the morphology and crystallographic orientation of the edges of the triangular etch pits is indicated).

The measured depth of shallow etch pits (about 0.5 nm) closely resembles the thickness of one unit-cell layer (0.47 nm) (Figure 1E). Moreover, according to the brucite sheet structure with edge-sharing $\text{Mg}(\text{OH})_6$ octahedra (Figure 1E), the equilateral triangular morphology of the etch pits results from the 3-fold rotation axis normal to the (001) cleavage surface.²⁹

When the brucite surface was exposed to 1 mM phytate solutions with 10 mM NaCl at pH 7.0, the pit depth gradually increased to about 6.0 nm after 28 min of reaction (Figure 2A, B). At the same time, spherical particles (2.0–16.0 nm in height) (Figure 2A, B) and 2-D plates (14.0–16.0 nm in thickness) (Figure 2A, C) formed. As the pH of the 1 mM phytate solutions was further decreased to 3.0, simultaneous occurrence of shallow and deep (>10 nm) dissolution pits was observed following 279 s of dissolution reactions (Figure 2D). Rows of etch pits associated with linear defects were evident on areas of the surface that remained free of precipitate (Arrows in Figure 2D, E). The brucite surface became heavily pitted after 360 s (Figure 2E), and finally, the surface was completely covered by nanoparticles (about 40–60 nm in height) after 497 s of dissolution (Figure 2F, F'). Dissolution and precipitation was occurring simultaneously in a coupled process at the brucite-solution interface.^{30,31} The dissolution of brucite releases Mg^{2+} ions to the interfacial solution in contact with the brucite surface, so that this solution boundary layer becomes supersaturated with respect to a new Mg-OP phase.

It is apparent that phytate-mediated brucite dissolution occurs via a different process depending on the pH range. Dissolution at point defects dominated at higher pH (>7.0), and at linear defects (including screw defects, line dislocations, and dislocation loops) at lower pH (<5.0) could be clearly imaged, similar to ligand-driven dissolution at linear defects on calcite.³² For blank solutions in the absence of any OP and pyrophosphate used in this study, typical brucite (001) surfaces dissolve very slowly by the formation and spreading of equilateral triangular etch pits in pure water.³³ Etch pit spreading rates in water increased with decreasing pH, from about 0.22 nm s^{-1} at pH 4– 0.70 nm s^{-1} at pH 2.³³ Above pH 8, the etch pit retreat velocities rapidly decreased from about 0.030 nm s^{-1} at pH 9 to virtually zero at pH 10–12.³³ This pH-dependent retreat velocity at pH < 7.0 is consistent with step velocities for water-promoted calcite dissolution,³⁴ and can be explained by considering that the dissolution rate of brucite is a function of the $> \text{MgOH}_2^+$ surface concentration (>indicates a surface site).^{33,35} Increasing H^+ activity results in enhanced protonation of $> \text{MgOH}^0$ surface sites and the formation of $> \text{MgOH}_2^+$, thus promoting brucite dissolution.³³ In addition, etch pit spreading is also promoted by the presence of background electrolytes such as NaHCO_3 at a constant pH.³³

Step velocity in the presence of phytate perceptibly increased as pits deepened (depth >10 nm in Figure 2D), although the relationship between step retreat velocity and pit depth and dependence on pH could not be determined in the present AFM experiments. The increase of step velocity in phytate solutions would have contributions from the shallower, slow-retreat pits at point defects promoted by water and the deeper, fast-retreat pits along linear defects promoted by organic ligands such as phytate. These observations are similar to those reported for the case of calcite dissolution in the presence of ethylenediamine tetraacetate (EDTA).³² Linear defects (such as dislocations) penetrate deeply into the mineral structure, resulting in deeper pits.^{32,36,37}

Coupled Dissolution–Precipitation at the Brucite–Solution Interface in the Presence of Pyrophosphate. In the presence of 1 mM pyrophosphate at pH 9.6 for 23 h, scarce isolated nanoparticles (about 2.0–6.0 nm) were formed along step edges on dissolving brucite surfaces, where dissolution occurred through the formation of typical equilateral triangular etch pits (Figure 3A, SI Figure S1A'). When the pH was

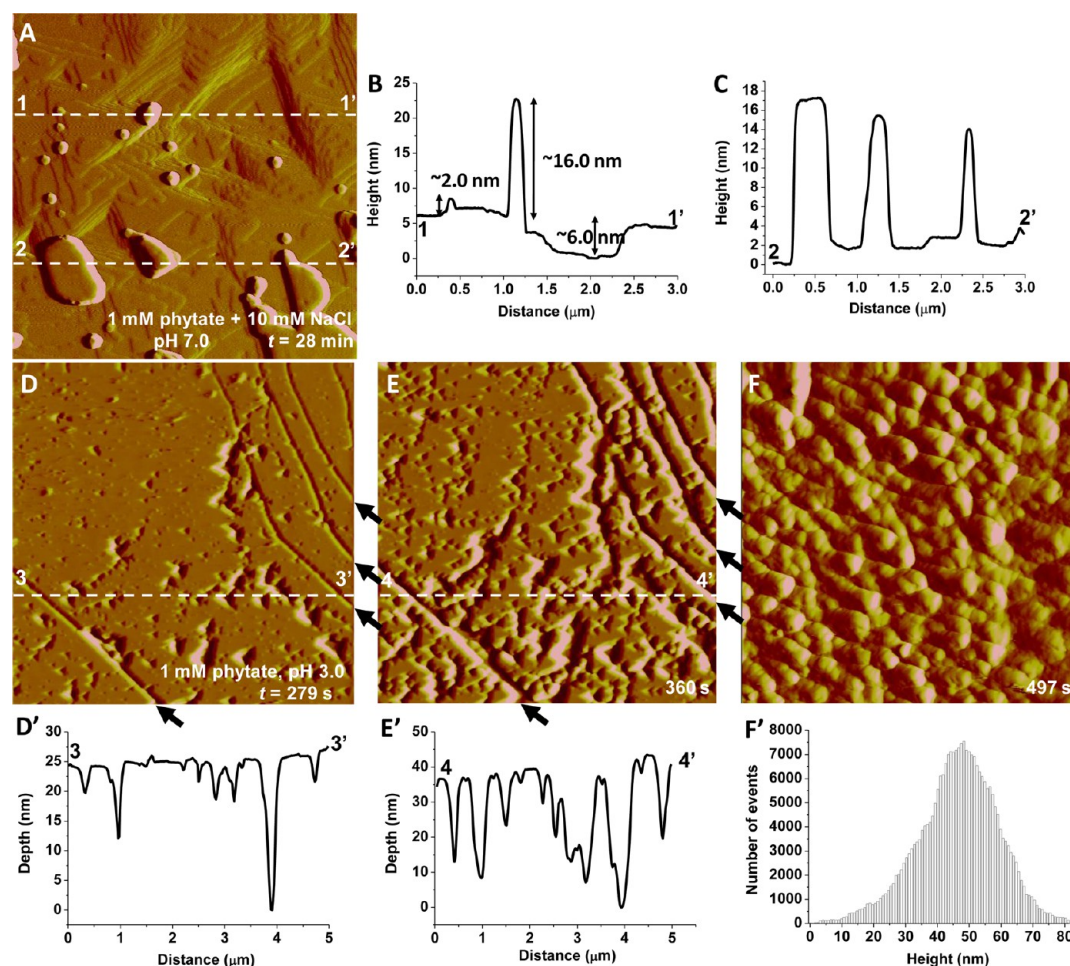


Figure 2. Time sequence AFM (deflection mode) images of brucite dissolution and precipitation in the presence of phytate. (A) In situ AFM images show both etch pit formation and precipitation on a brucite (001) surface in 1 mM phytate + 10 mM NaCl (pH 7.0) at $t = 28$ min. (B and C) Height profiles of nucleated nanoparticles (about 2–16 nm) and 2-D nanoplates (about 16 nm in thickness) along the dashed lines 1 \rightarrow 1' and 2 \rightarrow 2', respectively. (D and E) Time-resolved AFM images show the coexistence of point and line defects formed in 1 mM phytate (pH 3.0). Pits associated with observable line defects are apparent (Arrows). (D' and E') Depth profiles of etch pits and line defects along the dashed lines 3 \rightarrow 3' and 4 \rightarrow 4', respectively. (F) After 497 s, brucite substrates were covered by larger nanoparticles (about 50 nm in F'). Image A, $3 \times 3 \mu\text{m}$; D-F, $5 \times 5 \mu\text{m}$.

lowered to 7.0 and the pyrophosphate concentration was raised to 5 mM, some particles of size 10–20 nm were present after 43 min of brucite dissolution (Figure 3B, SI Figure S1B'). When the pH was further decreased to 4.3 in 1 mM pyrophosphate, the immediate formation of pits associated with linear defects (depths in 2.0–4.0 nm) was observed after 103 s of dissolution (Figure 3C, D, and SI Figure S1D'). Spherical particles (about 2.0–10.0 nm in height) (Figure 3E, SI Figure S1E') and conical precipitates (about 40.0–120.0 nm in height) (Figure 3F, SI Figure S1F') were formed after 192 s and 37 min, respectively.

Coupled Dissolution–Precipitation at the Brucite–Solution Interface in the Presence of G6P. In the presence of 1 mM G6P at pH 5.9, dissolution occurred with the formation of equilateral triangular etch pits on the brucite (001) surfaces, and their depth gradually increased from about 4.0 nm at 13 min, to about 8.0 nm at 41 min, and 8.0–10.0 nm at 81 min (Figure 4). At the same time, their sizes (width) also increased (Figure 4A'–C'). However, no precipitates were observed even after 17 h of ex situ reactions (SI Figure S2). As the G6P concentration was increased to 5 mM at pH 5.8, precipitates were formed after 18 h in ex situ reactions (SI Figure S3). When the pH of 5 mM G6P solutions was

decreased to 3.5, etch pits rapidly formed (Figure 5); the brucite surfaces were completely covered by particles (Figure 5) with a height of 40–50 nm (SI Figure S4A, B) after 16 h of dissolution reactions.

Dynamics of Nucleation and Growth of Mg-OP/PyroP on Brucite. The dissolving brucite surfaces in the presence of OPs and pyrophosphate provided a source of Mg^{2+} ions, resulting in supersaturation of the solution in the brucite–solution boundary layers with respect to an OP/PyroP-Mg phase.³⁸ This will drive surface-induced nucleation and growth on the brucite surface. According to classical nucleation theory (CNT), the steady-state nucleation rate (number of nucleation events per square meter per second), J , can be calculated as^{39,40}

$$J = A \exp\left(-\frac{\Delta G^*}{k_B T}\right) \quad (1)$$

where A is a kinetic constant, depending on physical parameters such as diffusional barriers,^{39,40} ΔG^* is the total free-energy cost to form a spherical crystallite, k_B is Boltzmann's constant, and T is temperature.^{39,40} The technical difficulties involved in directly evaluating crystal nucleation rates⁴¹ have led to an approach to measure the induction period (t) prior to

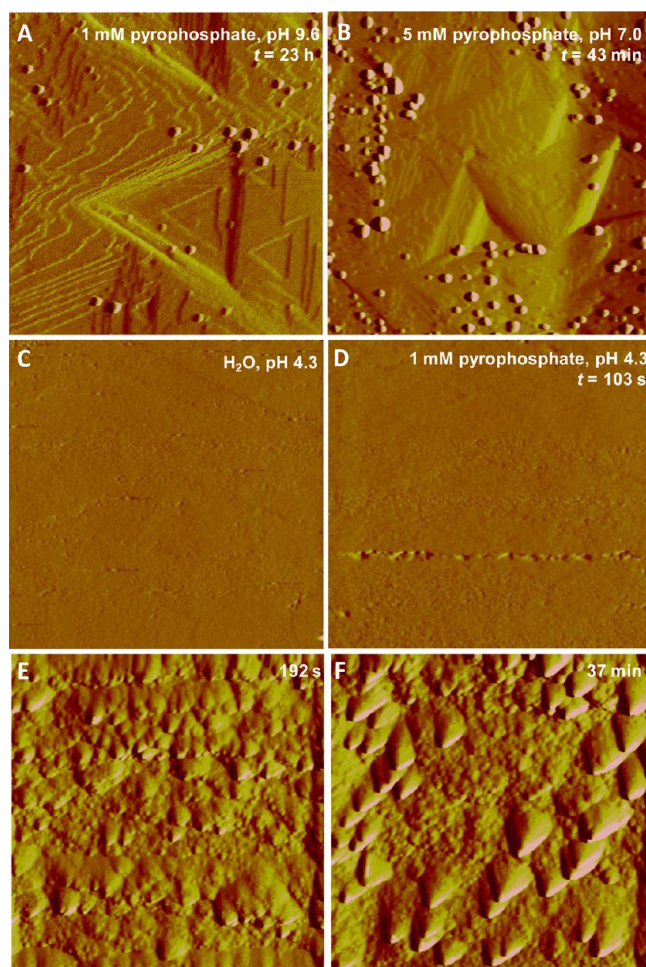


Figure 3. Time sequence AFM (deflection mode) images of brucite dissolution and precipitation in the presence of pyrophosphate. In situ AFM images show coupled dissolution (by etch pit formation) and precipitation on a brucite (001) surface in (A) 1 mM pyrophosphate (pH 9.6) at $t = 23$ h and (B) 5 mM pyrophosphate (pH 7.0) at $t = 43$ min. Time-resolved AFM images show (C and D) the formation of pits associated with line defects, and (E and F) spherical particles and conical precipitates in 1 mM pyrophosphate (pH 4.3). Images A and C–F, $3 \times 3 \mu\text{m}$; B, $5 \times 5 \mu\text{m}$.

nucleation based on the equation $J = 1/(tV)$,⁴¹ where V is the volume of the entire system (i.e., fluid + crystal, about $50 \mu\text{L}$). In the present study, we used the time required to observe the occurrence of the first smallest particles (about 2.0–6.0 nm in height) on brucite to characterize the kinetics of nucleation. Moreover, we only compared the induction times for phytate and pyrophosphate solutions on brucite surfaces because a relatively longer time was required to form nucleated particles for solutions containing G6P (SI Figure S2). The most likely explanation for delayed nucleation in GP6 solutions is that G6P contains the lowest number of phosphate groups (1) compared to the other two molecules tested, 2() and hence indicates a lower chelation ability. The induction time significantly increased with the increase in pH for both phytate and pyrophosphate solutions at 1 mM, and at the same alkaline pH, the induction time for pyrophosphate (1 mM) is much longer than that of phytate (1 mM) (Figure 6A). Shorter induction times were observed with increasing phytate or pyrophosphate solution concentration (Figure 6B) or NaCl concentration (in

1 mM phytate or pyrophosphate) (Figure 6C) when the solution pH was kept constant (7.0).

Mineral dissolution kinetics is complicated in the presence of inorganic/organic ligands⁴² and background electrolytes.^{34,43} Background electrolytes can enhance the mineral dissolution rate due to the ability of salt ions to modify water structure as well as solute and mineral surface hydration.^{43,44} The amount of released Mg^{2+} ions by dissolution is increased in the presence of NaCl, thereby resulting in rapid nucleation of a Mg-OP/PyroP phase with shorter induction times because a higher degree of supersaturation is reached within the boundary layers. This phenomenon has also been observed in the calcite-G6P system.⁴⁴

Identification of Precipitates on Brucite (001) Cleavage Surfaces. Using Raman spectroscopy, the cleaved brucite surface shows two sharp, intense peaks at 281 and 446 cm^{-1} and two broad peaks with centers at 725 and 809 cm^{-1} (Figure 7A). This is consistent with previous analysis of brucite using spectroscopic methods.⁴⁵ In contrast, precipitates on the brucite surface show additional peaks depending on the organophosphate present in the experiment solution. In experiments with G6P, the precipitates were highly reactive to the laser beam and even at the lowest laser intensity were burnt during analysis. However, the burnt material produced broad peaks at 1332 and 1575 cm^{-1} (Figure 7B) that are characteristic for amorphous carbon material⁴⁶ implying the original material was carbon-bearing, consistent with the precipitation of an organic-C phase during the experiments. Precipitates on the surface of brucite produced during the phytate experiments were stable in the Raman laser and produced clear peaks in the Raman spectra (Figure 7C). Additional peaks were observed as a broad peak at 544 cm^{-1} , three sharp and one broad peak at 954 , 993 , 1034 , and 1100 cm^{-1} and two broad bands at 1282 and 1372 cm^{-1} . These peaks are consistent with known Raman peaks for solid samples of phytate^{47,48} and particularly those between 950 and 1100 cm^{-1} are related to the symmetrical stretch of the phosphate moiety within the phytate molecule. However, the peaks are consistently shifted to higher wavenumbers in comparison to previous studies by as much as 10 cm^{-1} compared to the initial sodium salt.⁴⁹ Such a shift could imply a difference in chemistry of the precipitates through the incorporation of Mg released from the dissolving brucite, as Mg–acetate has been found to show a shift to higher wavenumbers in comparison to the Na–acetate salt.⁵⁰ No additional bands to those belonging to brucite were observed on the pyrophosphate sample surface. This can be explained from the SEM observations because the precipitate forms very thin, spread out crystals on the surface (SI Figure S5). In this case the laser beam would not sample enough of the precipitate during Raman analysis to produce bands in the spectra, precluding any possible identification of other vibrational peaks from any nanometer thin precipitate layer.

PHREEQC Simulations. Finally, we calculated the solution speciation using thermodynamic constants (SI Table S1–S7) during brucite dissolution in the presence of 1.0 mM phytate at pH 2.5 and 7.0 by PHREEQC.²⁸ This allowed simulations of brucite dissolving until equilibrium. The simulations show that for both initial pH values, the solution (volume of solution is equivalent to that of the AFM fluid cell, about 35 – $50 \mu\text{L}$) would reach supersaturation with respect to $\text{Mg}_3\text{H}_2\text{Phytate} \cdot 6\text{H}_2\text{O}$ as a Mg-phytate phase (SI Data 1 and 2). This is consistent with the AFM results (Figure 2). For the

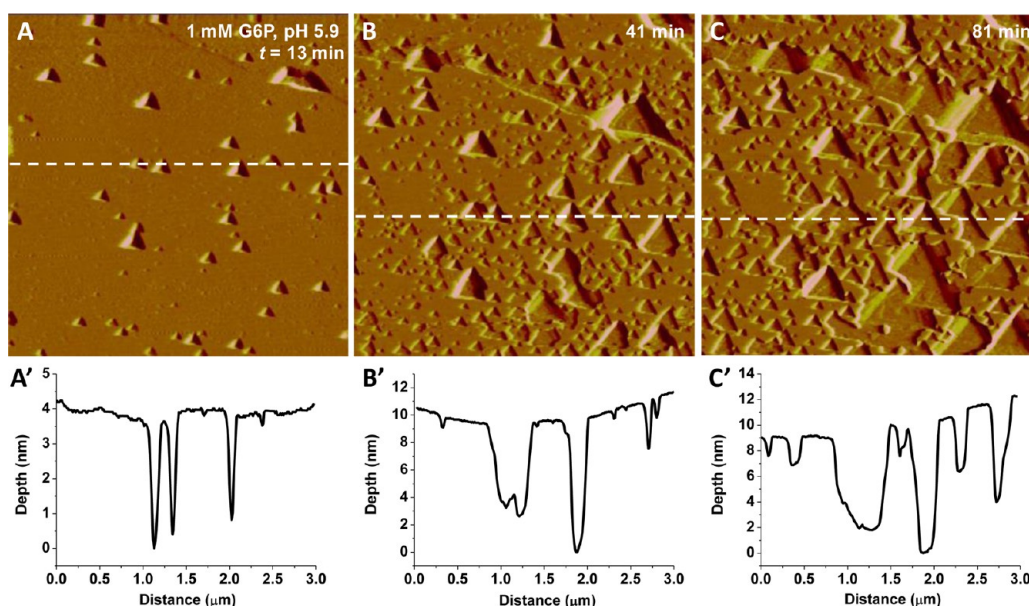


Figure 4. Time sequence AFM (deflection mode) images of brucite dissolution in the presence of G6P. (A–C) In situ AFM images of a brucite (001) surface dissolving in 1 mM G6P (pH 5.9). (A'–C') Depth profiles of the etch pits evaluated along the white dashed lines in A–C. Images A–C, $3 \times 3 \mu\text{m}$.

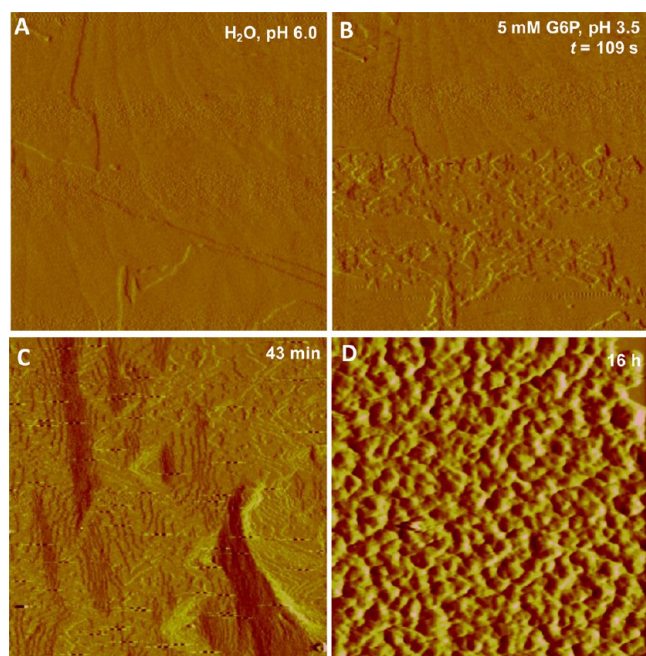


Figure 5. Time-resolved AFM (deflection mode) images of brucite dissolution and precipitation in the presence of G6P. In situ AFM images show both (A–C) etch pit formation and evolution, and (D) precipitation on a brucite (001) surface in 5 mM G6P (pH 3.5). After 16 h, brucite substrates were covered by larger nanoparticles. Images A–D, $3 \times 3 \mu\text{m}$.

pyrophosphate system (1.0 mM) at more acidic pH (4.3) the solution reaches saturation with respect to $\text{Mg}_2\text{P}_2\text{O}_7$ as a Mg-pyrophosphate phase, that may become stable before equilibrium with brucite is attained (SI Data 3). At $\text{pH} \geq 7.0$, the solution is saturated with respect to brucite before saturation with respect to $\text{Mg}_2\text{P}_2\text{O}_7$ is attained (SI Data 4 and 5). This means for the formation of $\text{Mg}_2\text{P}_2\text{O}_7$ at higher pH more brucite would need to dissolve (to release enough Mg^{2+})

through the addition of higher pyrophosphate concentrations and/or longer reaction times. These simulation results are also consistent with the AFM observations (Figure 3). Moreover, we made further simulations for the same solutions of 1.0 mM phytate and pyrophosphate at a fixed pH of 4.3 or 7.0, while allowing the pH to vary as brucite dissolved. Results showed that both $\text{Mg}_5\text{H}_2\text{Phytate} \cdot 6\text{H}_2\text{O}$ and $\text{Mg}_2\text{P}_2\text{O}_7$ become thermodynamically stable due to the solutions reaching supersaturation with respect to these two phases (SI Data 6–8). Because it is impossible to include all possible species in the database and appropriate equilibrium constants are mostly lacking, the simulations are incomplete, especially for the formation of other solid phases, for example hydrated $\text{Mg}_2\text{P}_2\text{O}_7$.

Due to the limitation of appropriate thermodynamic data, all PHREEQC simulations were an approximation to the real scenario. However, the simulations predicted the fast formation of a Mg-phytate phase at the pH values tested. The Mg-Pyrophosphate phase did not form at $\text{pH} \geq 7$ and only became significant at lower pH values when dissolution of brucite was enhanced. This is in accordance with the AFM observations and Raman analyses, especially, as Raman analyses for ex situ formation of precipitates on the surface of brucite verify the utility of speciation modeling. The lack of equilibrium constant data did not allow for simulations with G6P.

In summary, from our observations a higher number of phosphate groups in a phosphate molecule seems to enhance the chelating ability of the molecule to sequester Mg^{2+} . The reaction rates of dissolution and subsequent precipitation followed the order: phytate (with six phosphate groups per molecule) > pyrophosphate (two phosphate groups) > G6P (one phosphate group) at all pH values tested.

Implications. A fundamental challenge in the study of soil organic and inorganic phosphate dynamics is to assess the relative importance of adsorption and precipitation processes on mineral surfaces in the environment as this plays an important role in the global P cycle.⁴⁴ In this study, direct AFM observations and kinetic analyses have been applied to observe

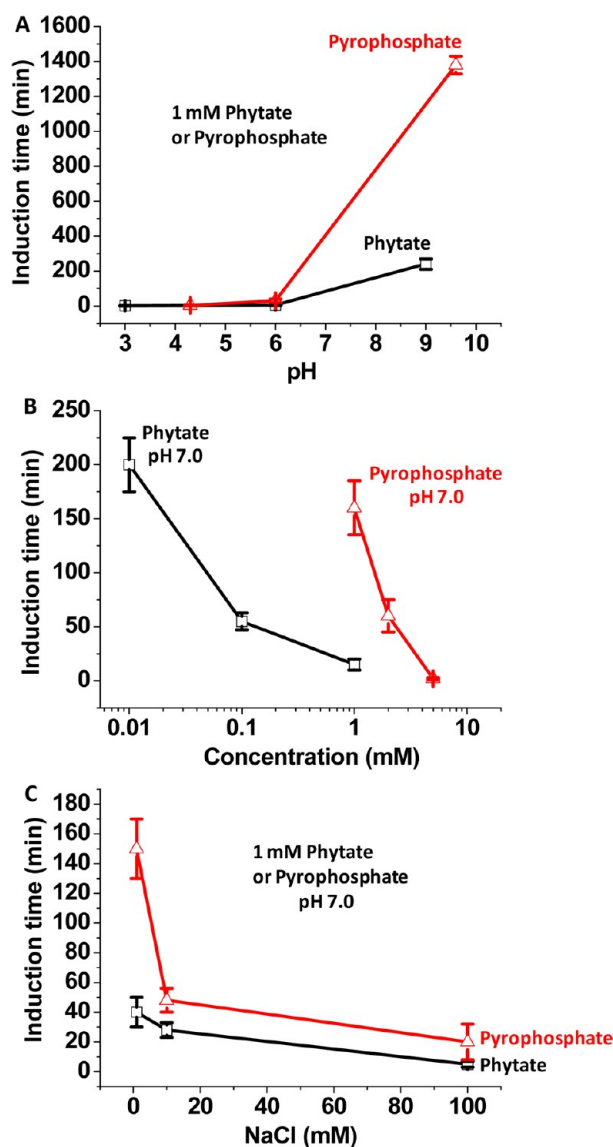


Figure 6. Induction times for precipitate formation on the brucite (001) surfaces under various experimental conditions in the presence of phytate or pyrophosphate. (A) A range of pH values, (B) Phytate or pyrophosphate concentrations at pH 7.0, and (C) NaCl concentrations with 1 mM phytate or pyrophosphate at pH 7.0. Induction times are reported as mean \pm SD.

and predict the behavior of OPs and PyroP on brucite mineral surfaces. Our results may provide dynamic insights into how OP and PyroP can be sequestered through mineral interfacial dissolution–precipitation reactions.⁵¹ The approach used in this study may readily extend to further investigate the adsorption and precipitation dynamics of guest anions/cations on the surfaces and in the interlayer spaces in brucite-like minerals such as hydrotalcite-like layered double hydroxides (LDHs).⁵² These minerals are of considerable environmental relevance because of their anion-exchange capacity that can affect the mobility of chemical species and removal of toxic anions.⁵² Moreover, these materials can accommodate a wide range of different cations in the interlayer spaces for use in environmental remediation of heavy metals.^{52,53}

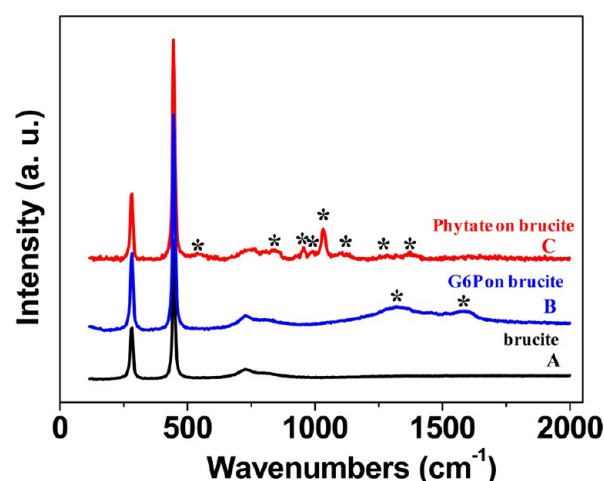


Figure 7. Raman spectra taken from (A) brucite, and surface precipitates from an AFM experiment run with (B) G6P or (C) phytate. Asterisks indicate peaks unrelated to the underlying brucite generated by the surface precipitates in the different organic phosphate experiments.

■ ASSOCIATED CONTENT

Supporting Information

The Supporting Information is available free of charge on the ACS Publications website at DOI: 10.1021/acs.est.6b05456.

AFM images and depth profiles of brucite dissolution and precipitation in the presence of pyrophosphate (Figure S1); ex situ reaction of 1 mM G6P with brucite (Figure S2); ex situ reaction of 5 mM G6P with brucite (Figure S3); depth profile of brucite substrates covered by larger nanoparticles in 5 mM G6P at pH 3.5 (Figure S4); SEM images of brucite with OPs under different reaction conditions (Figure S5); Protonation constants for phytate (Table S1); Association constants for Mg-phytate complexes (Table S2). Solubility constants of possible solid phases (Mg-phytate) (Table S3). Protonation constants for pyrophosphate (PyroP) (Table S4). Association constants for Na-pyrophosphate complexes (Table S5). Association constants for Mg-pyrophosphate complexes (Table S6). Solubility constants of possible solid phases (Mg-PyroP) (Table S7), and PHREEQC calculations (Supporting Data 1–8) (PDF)

■ AUTHOR INFORMATION

Corresponding Authors

*(L.W.) Phone/fax: +86-27-87288382; e-mail: ljwang@hzau.edu.cn.

*(C.V.P.) Phone: +49-251-8333454; fax: +49-251-8338397; e-mail: putnisc@uni-muenster.de.

ORCID

Lijun Wang: 0000-0001-7125-9480

Jörn Hövelmann: 0000-0002-1961-653X

Notes

The authors declare no competing financial interest.

■ ACKNOWLEDGMENTS

This work was supported by the National Natural Science Foundation of China (41471245 and 41071208), a Specialized Research Fund for the Doctoral Program of Higher Education (20130146110030), and the Fundamental Research Funds for

the Central Universities (2662015PY206, 2662015PY116). C.V. Putnis and A. Putnis acknowledge support through EU Marie Curie initial training networks (FlowTrans and CO2 React). E.R.-A. acknowledges a Ramón y Cajal grant and support from the Research Group RNM-179 of the Junta de Andalucía.

REFERENCES

- (1) Baldwin, D. S. Organic phosphorus in the aquatic environment. *Environ. Chem.* **2013**, *10*, 439–454.
- (2) Turner, B. L.; Frossard, E.; Baldwin, D. S. *Organic Phosphorus in the Environment*; CABI Publishing: Cambridge, 2005.
- (3) Dyhrman, S.; Chappell, P.; Haley, S.; Moffett, J.; Orchard, E.; Waterbury, J.; Webb, E. Phosphonate utilization by the globally important marine diazotroph *Trichodesmium*. *Nature* **2006**, *439*, 68–71.
- (4) Zhu, Y. R.; Wu, F. C.; He, Z. Q.; Guo, J. Y.; Qu, X. X.; Xie, F. Z.; Giesy, J. P.; Liao, H. Q.; Guo, F. Characterization of organic phosphorus in lake sediments by sequential fractionation and enzymatic hydrolysis. *Environ. Sci. Technol.* **2013**, *47*, 7679–7687.
- (5) Lu, C.; Wang, B.; He, J.; Vogt, R. D.; Zhou, B.; Guan, R.; Zuo, L.; Wang, W.; Xie, Z.; Wang, J.; Yan, D. Responses of organic phosphorus fractionation to environmental conditions and lake evolution. *Environ. Sci. Technol.* **2016**, *50*, 5007–5016.
- (6) Ahlgren, J.; Tranvik, L.; Gogoll, A.; Waldebäck, M.; Markides, K.; Rydin, E. Sediment depth attenuation of biogenic phosphorus compounds measured by ^{31}P NMR. *Environ. Sci. Technol.* **2005**, *39*, 867–872.
- (7) Cade-Menun, B. J.; Navaratnam, J. A.; Walbridge, M. R. Characterizing dissolved and particulate phosphorus in water with ^{31}P nuclear magnetic resonance spectroscopy. *Environ. Sci. Technol.* **2006**, *40*, 7874–7880.
- (8) McLaren, T. I.; Smernik, R. J.; McLaughlin, M. J.; McBeath, T. M.; Kirby, J. K.; Simpson, R. J.; Guppy, C. N.; Doolette, A. L.; Richardson, A. E. Complex forms of soil organic phosphorus—A major component of soil phosphorus. *Environ. Sci. Technol.* **2015**, *49*, 13238–13245.
- (9) Sims, J. T.; Pierzynski, G. M. Chemistry of Phosphorus in Soils. In *Chemical Processes in Soils*; Tabatabai, M. A., Sparks, D. L., Eds.; Soil Science Society of America: Madison, WI, 2005; pp 151–192.
- (10) Turner, B. L.; Cheesman, A. W.; Godage, H. Y.; Riley, A. M.; Potter, B. V. L. Determination of *neo*- and *D-chiro*-inositol hexakisphosphate in soils by solution ^{31}P NMR spectroscopy. *Environ. Sci. Technol.* **2012**, *46*, 4994–5002.
- (11) Azeem, M.; Riaz, A.; Chaudhary, A. N.; Hayat, R.; Hussain, Q.; Tahir, M. I.; Imran, M. Microbial phytase activity and their role in organic P mineralization. *Arch. Agron. Soil Sci.* **2015**, *61*, 751–766.
- (12) Turner, B. L.; Paphazy, M. J.; Haygarth, P. M.; McKelvie, I. D. Inositol phosphates in the environment. *Philos. Trans. R. Soc., B* **2002**, *357*, 449–469.
- (13) Thavarajah, P.; Thavarajah, D.; Vandenberg, A. Low phytic acid lentils (*Lens culinaris* L.): a potential solution for increased micronutrient bioavailability. *J. Agric. Food Chem.* **2009**, *57*, 9044–9049.
- (14) Tu, S. X.; Ma, L.; Luongo, T. Root exudates and arsenic accumulation in arsenic hyperaccumulating *Pteris vittata* and non-hyperaccumulating *Nephrolepis exaltata*. *Plant Soil* **2004**, *258*, 9–19.
- (15) Liu, X.; Fu, J. W.; Guan, D. X.; Cao, Y.; Luo, J.; Rathinasabapathi, B.; Chen, Y. S.; Ma, L. Q. Arsenic induced phytate exudation, and promoted FeAsO_4 dissolution and plant growth in As-hyperaccumulator *Pteris vittata*. *Environ. Sci. Technol.* **2016**, *50*, 9070–9077.
- (16) Espinosa, M.; Turner, B. L.; Haygarth, P. M. Preconcentration and separation of trace phosphorus compounds in soil leachate. *J. Environ. Qual.* **1999**, *28*, 1497–1504.
- (17) Huang, R. X.; Tang, Y. Z. Speciation dynamics of phosphorus during (hydro)thermal treatments of sewage sludge. *Environ. Sci. Technol.* **2015**, *49*, 14466–14474.
- (18) Paytan, A.; Cade-Menun, B. J.; McLaughlin, K.; Faul, K. L. Selective phosphorus regeneration of sinking marine particles: evidence from ^{31}P NMR. *Mar. Chem.* **2003**, *82*, 55–70.
- (19) Sundareshwar, P. V.; Morris, J. T.; Pellechia, P. J.; Cohen, H. J.; Porter, D. E.; Jones, B. C. Occurrence and implications of pyrophosphate in estuaries. *Limnol. Oceanogr.* **2001**, *46*, 1570–1577.
- (20) Cade-Menun, B. J. *Organic Phosphorus in the Environment*; CABI Publishing: Oxon, U.K., 2005.
- (21) Selig, U.; Hübener, T.; Michalik, M. Dissolved and particulate phosphorus forms in a eutrophic shallow lake. *Aquat. Sci.* **2002**, *64*, 97–105.
- (22) Nöges, P.; Tuvikene, L.; Nöges, T.; Kisand, A. Primary production, sedimentation and resuspension in large shallow Lake Võrtsjärv. *Aquat. Sci.* **1999**, *61*, 168–182.
- (23) Shinohara, R.; Imai, A.; Kawasaki, N.; Komatsu, K.; Kohzu, A.; Miura, S.; Sano, T.; Satou, T.; Tomioka, N. Biogenic phosphorus compounds in sediment and suspended particles in a shallow eutrophic lake: A ^{31}P -nuclear magnetic resonance study. *Environ. Sci. Technol.* **2012**, *46*, 10572–10578.
- (24) Shinohara, R.; Imai, A.; Kohzu, A.; Tomioka, N.; Furusato, E.; Satou, T.; Sano, T.; Komatsu, K.; Miura, S.; Shimotori, K. Dynamics of particulate phosphorus in a shallow eutrophic lake. *Sci. Total Environ.* **2016**, *563–564*, 413–423.
- (25) Condron, L. M.; Turner, B. L.; Cade-Menun, B. J. Chemistry and dynamics of soil organic phosphorus. In *Phosphorus: Agriculture and the Environment*; Sims, T., Sharpley, A. N., Eds.; American Society of Agronomy: Madison, WI, 2005; pp 87–121.
- (26) Turner, B. L.; Newman, S.; Ramesh Reddy, K. Overestimation of organic phosphorus in wetland soils by alkaline extraction and molybdate colorimetry. *Environ. Sci. Technol.* **2006**, *40*, 33493–3354.
- (27) Turner, B. L.; Frossard, E.; Baldwin, D. S. *Organic Phosphorus in the Environment*; CAB International: Wallingford, CT, 2005.
- (28) Parkhurst, D. L.; Appelo, C. A. J. Users guide to PHREEQC (Version 3). In *A Computer Program for Speciation, Batch-Reaction, One-Dimensional Transport, and Inverse Geochemical Calculations*; U.S. Geological Survey Techniques and Methods: Washington, DC, 2013.
- (29) Kudoh, Y.; Kameda, J.; Kogure, T. Dissolution of brucite on the (001) surface at neutral pH: in situ atomic force microscopy observations. *Clays Clay Miner.* **2006**, *54*, 598–604.
- (30) Putnis, A. Mineral replacement reactions. In: Oelkers, E. H., Schott, J. (Eds.), *Thermo- dynamics and Kinetics of Water–Rock Interaction*. *Rev. Mineral. Geochem.* **2009**, *30*, 87–124.10.2138/rmg.2009.70.3
- (31) Ruiz-Agudo, E.; Putnis, C. V.; Putnis, A. Coupled dissolution and precipitation at mineral–fluid interfaces. *Chem. Geol.* **2014**, *383*, 132–146.
- (32) Perry, T. D.; Duckworth, O. W.; Kendall, T. A.; Martin, T. A.; Mitchell, R. Chelating ligand alters the microscopic mechanism of mineral dissolution. *J. Am. Chem. Soc.* **2005**, *127*, 5744–5745.
- (33) Hövelmann, J.; Putnis, C. V.; Ruiz-Agudo, E.; Austrheim, H. Direct nanoscale observations of CO_2 sequestration during brucite $[\text{Mg}(\text{OH})_2]$ dissolution. *Environ. Sci. Technol.* **2012**, *46*, 5253–5260.
- (34) Wang, L. J.; Ruiz-Agudo, E.; Putnis, C. V.; Menneken, M.; Putnis, A. Kinetics of calcium phosphate nucleation and growth on calcite: Implications for predicting the fate of dissolved phosphate species in alkaline soils. *Environ. Sci. Technol.* **2012**, *46*, 834–842.
- (35) Pokrovsky, O. S.; Schott, J. Experimental study of brucite dissolution and precipitation in aqueous solutions: surface speciation and chemical affinity control. *Geochim. Cosmochim. Acta* **2004**, *68*, 31–45.
- (36) MacInnis, I. N.; Brantley, S. L. The role of dislocations and surface morphology in calcite dissolution. *Geochim. Cosmochim. Acta* **1992**, *56*, 1113–1126.
- (37) Duckworth, O. W.; Martin, S. T. Dissolution rates and pit morphologies of rhombohedral carbonate minerals. *Am. Mineral.* **2004**, *89*, 554–563.
- (38) Putnis, A. Why mineral interfaces matter. *Science* **2014**, *343*, 1441–1442.

- (39) Liu, X. Y.; Lim, S. W. Templating and supersaturation driven anti-templating: Principles of biominerals architecture. *J. Am. Chem. Soc.* **2003**, *125*, 888–895.
- (40) Nielsen, A. E. *Kinetics of Precipitation*; Pergamon: Oxford, U.K., 1964.
- (41) Wang, L. J.; Guan, X.; Tang, R.; Hoyer, J. R.; Wierzbicki, A.; De Yoreo, J. J.; Nancollas, G. H. Phosphorylation of osteopontin is required for inhibition of calcium oxalate crystallization. *J. Phys. Chem. B* **2008**, *112*, 9151–9157.
- (42) Qin, L. H.; Zhang, W. J.; Lu, J. W.; Stack, A. G.; Wang, L. J. Direct imaging of nanoscale dissolution of dicalcium phosphate dihydrate by an organic ligand: Concentration matters. *Environ. Sci. Technol.* **2013**, *47*, 13365–13374.
- (43) Ruiz-Agudo, E.; Kowacz, M.; Putnis, C. V.; Putnis, A. The role of background electrolytes on the kinetics and mechanism of calcite dissolution. *Geochim. Cosmochim. Acta* **2010**, *74*, 1256–1267.
- (44) Wang, L. J.; Qin, L. H.; Putnis, C. V.; Ruiz-Agudo, E.; King, H. E.; Putnis, A. Visualizing organophosphate precipitation at the calcite-water interface by in situ atomic-force microscopy. *Environ. Sci. Technol.* **2016**, *50*, 259–268.
- (45) Dawson, P.; Hadfield, C. D.; Wilkinson, G. R. The polarized infra-red and Raman spectra of $\text{Mg}(\text{OH})_2$ and $\text{Ca}(\text{OH})_2$. *J. Phys. Chem. Solids* **1973**, *34*, 1217–1225.
- (46) Ferrari, A. C.; Robertson, J. Interpretation of Raman spectra of disordered and amorphous carbon. *Phys. Rev. B: Condens. Matter Mater. Phys.* **2000**, *61*, 14095–14107.
- (47) Kolozsvari, B.; Firth, S.; Saiardi, A. Raman spectroscopy detection of phytic acid in plant seeds reveals the absence of inorganic polyphosphate. *Mol. Plant* **2015**, *8*, 826–828.
- (48) Yang, H. F.; Feng, J.; Liu, Y. L.; Yang, Y.; Zhang, Z. R.; Shen, G. L.; Yu, R. Q. Electrochemical and surface enhanced Raman scattering spectroelectrochemical study of phytic acid on the silver electrode. *J. Phys. Chem. B* **2004**, *108*, 17412–17417.
- (49) Yang, H.; Yang, Y.; Yang, Y.; Liu, H.; Zhang, Z.; Shen, G.; Yu, R. Formation of inositol hexaphosphate monolayers at the copper surface from a Na-salt of phytic acid solution studied by in situ surface enhanced Raman scattering spectroscopy, Raman mapping and polarization measurements. *Anal. Chim. Acta* **2005**, *458*, 150–165.
- (50) Frost, R. L.; Klopogge, J. T. Raman spectroscopy of the acetates of sodium, potassium and magnesium at liquid nitrogen temperature. *J. Mol. Struct.* **2000**, *526*, 131–141.
- (51) Putnis, C. V.; Ruiz-Agudo, E. The mineral-water interface: where minerals react with the environment. *Elements* **2013**, *9*, 177–182.
- (52) Sideris, P. J.; Nielsen, U.; Gan, Z.; Grey, C. P. Mg/Al ordering in layered double hydroxides revealed by multinuclear NMR spectroscopy. *Science* **2008**, *321*, 113–117.
- (53) Liang, X.; Zang, Y.; Xu, Y.; Tan, X.; Hou, W.; Wang, L.; Sun, Y. Sorption of metal cations on layered double hydroxides. *Colloids Surf., A* **2013**, *433*, 122–131.